Meridional Heat Transport in the DeepMIP Eocene ensemble: non-CO_2 and CO_2 effects

Fanni Dora Kelemen[1], Sebastian Steinig[2], Agatha de Boer[3], Jiang Zhu[4] , Wing-Le Chan[5], Igor Niezgodzki[6], David K. Hutchinson[7], Gregor Knorr[8], Ayako Abe-Ouchi[5], Bodo Ahrens[1]

[1]Institute for Atmospheric and Environmental Sciences, Goethe University Frankfurt, Germany,

[2]School of Geographical Sciences, University of Bristol, Bristol, UK,

[3]Department of Geological Sciences, Bolin Centre for Climate Research, Stockholm University, Stockholm, Sweden,

[4]Climate and Global Dynamics Laboratory, National Center for Atmospheric Research, Boulder, Colorado, USA

[5]AORI, The University of Tokyo, Kashiwa, Japan,

[6]ING PAN - Institute of Geological Sciences Polish Academy of Sciences, Research Center in Kraków, Biogeosystem Modelling Group, Kraków, Poland

[7]Climate Change Research Centre, University of New South Wales Sydney, Australia

[8]Alfred Wegener Institute, Helmholtz Centre for Polar and Marine Research, Bremerhaven, Germany,

Corresponding author: Fanni D. Kelemen (kelemen@iau.uni-frankfurt.de)

Key Points:

- The latent heat transport of the monsoon systems increases through higher CO_2 concentration, but it is reduced by the Eocene topography.
- The poleward heat transport of midlatitude cyclones is higher in the Northern Hemisphere in the Eocene, due to the different topography.
- The Hadley cells are overturning more heat in response to the higher CO_2 values, but the net poleward heat transport is relatively stable.

Abstract

The total meridional heat transport (MHT) is relatively stable across different climates. Nevertheless, the strength of individual processes contributing to the total transport are not stable. Here we investigate the MHT and its main components especially in the atmosphere, in five coupled climate model simulations from the Deep-Time Model Intercomparison Project (DeepMIP). These simulations target the Early Eocene Climatic Optimum (EECO), a geological time period with high CO_2 concentrations, analogous to the upper range of end-of-century CO_2 projections. Preindustrial and early Eocene simulations at a range of CO_2 levels (1x, 3x and 6x preindustrial values) are used to quantify the MHT changes in response to both CO_2 and non-CO_2 related forcings. We found that atmospheric poleward heat transport increases with CO_2, while the effect of non-CO_2 boundary conditions (e.g., paleogeography, land ice, vegetation) is causing more poleward atmospheric heat transport on the Northern and less on the Southern Hemisphere. The changes in paleogeography increase the heat transport via transient eddies at the mid-latitudes in the Eocene. The Hadley cells have an asymmetric response to both the CO_2 and non-CO_2 constraints. The poleward latent heat transport of monsoon systems increases with rising CO_2 concentrations, but this effect is offset by the Eocene topography. Our results show that the changes in the monsoon systems' latent heat transport is a robust feature of CO_2 warming, which is in line with the currently observed precipitation increase of present day monsoon systems.

Plain Language Summary

In the Earth's climate system both the atmosphere and the ocean are transporting heat through different processes from the tropics towards the poles. We investigate the transport of the atmosphere in several climate model set ups, which are aiming to describe the very warm climate of the early Eocene (~56-48 Myr ago). This period is relevant for us, because the atmospheric CO_2 concentration was close to our pessimistic projection of CO_2 concentration for the end of the century. In our study we are separating the results depending on their origin, meaning if the changes, seen in the heat transport are due to the larger CO_2 concentration or due to the different set up of the Eocene. We found that with rising CO_2 values the atmosphere transports more heat from the tropics to the polar regions. The different location of the continents and seas is influencing the heat transport of the midlatitude cyclones. The monsoon systems seem to be affecting a globally smaller area in the Eocene, but being more effective in transporting heat due to the higher atmospheric CO_2 concentration. This conclusion is in line with the observation, that current day monsoon systems' precipitation increases, as our CO_2 concentration rises.

1 Introduction

The meridional temperature gradient is the main driving force of the atmospheric and oceanic general circulation. It is caused by differential radiative heating and leads to meridional heat transport from the tropics to the mid- and high latitudes. It has been shown that the Meridional Heat Transport (MHT) is stable in different climate states (Krapp & Jungclaus, 2011; Smith et al., 2006; Yang et al., 2015). Bjerknes (1964) proposed that if the net radiation forcing at the top of the atmosphere (TOA) and the ocean heat storage do not vary too much, then the

MHT shall be also relatively stable. This leads to the expectation that any large variations in heat transport in the atmosphere and in the ocean should be equal in magnitude and opposite in sign, nevertheless it does not rule out large changes in both ocean and atmosphere. This mechanism since have been known as the Bjerknes compensation (BJC). Stone (1978) later showed that the MHT is mainly determined by the solar constant, the axial tilt, the radius of the Earth and the mean planetary albedo. Among these variables only the albedo is an internal parameter of the atmosphere-ocean system, and it highly depends on temperature, as a defining factor on clouds, ice and snow. Different modelling studies suggest that the BJC is valid in different paleo climate states, for example during the glacial-interglacial period of the last 22 000 years (Yang et al., 2015), or in the warm climate of the Middle Miocene (Krapp & Jungclaus, 2011). Also, it was found in preindustrial and in historical simulations of CMIP5 models, where in the latter, the climate is not in equilibrium and external forcings are present (Outten et al., 2018). Even in extreme theoretical cases, such as the aqua-planet, BJC is shown to be valid (Smith et al., 2006).

Even though total MHT is stable in different climate states, the contributions from various transport processes might change. Quantifying transport processes is a great tool to identify the large scale features of different climate states and reveal any compensating mechanism. In the climate system the heat is transported by the atmosphere and the ocean via different mechanisms. In the tropical belt both the atmosphere and the ocean contribute to the MHT equally, while at higher latitudes the atmospheric transport dominates (Masuda, 1988). At lower latitudes the heat is transported mainly by the meridional overturning circulation (MOC), which is represented by the Hadley cell in the atmosphere and by the wind-driven gyres in the upper ~1000 m of the ocean (Held, 2001). Note that we do not evaluate separately the role of the ocean's meridional overturning circulation so that MOC hereafter refers always to the atmosphere in this study. At higher latitudes the heat is transported dominantly by the atmosphere via different eddies, such as transient eddies (TE), comprised mainly of mid-latitude cyclones, and stationary eddies (SE), which represent monsoons in the subtropics and planetary waves in midlatitudes. The stationary planetary waves are connected to diverse topography and land-sea thermal contrast (Wills et al., 2019).

Change in the different transport processes have been shown to be relevant in the present climate, for example the changes in the poleward atmospheric and oceanic heat transport has been shown to contribute to the polar amplification (Forster et al., 2021). In a warmer climate the equator-to-pole gradient of atmospheric moisture is expected to increase due to the exponentially increasing water holding capacity of warmer air. The larger moisture gradient enhances the poleward latent heat transport. This process plays an important role in polar amplification. The polar amplification on the other hand results in a weakening of the equator-to-pole temperature gradient, which decreases the dry-static energy transport, what in turn partly compensates the increase in latent heat transport (Forster et al., 2021).The latest IPCC report shows that in our current warming climate large scale circulation patterns such as the Hadley cell or the monsoon systems have been changing (Gulev et al., 2021). Regarding the Hadley circulation the studies mostly indicate changes in the northern Hadley cell, in the form of widening and strengthening of the circulation (Gulev et al., 2021). The North Hemisphere summer monsoon precipitation shows an increase in the recent past (Gulev et al., 2021).

Investigating the large scale circulation trough, the transport processes in a past warm period of Earth’s climate system can help to better understand our future in a warmer climate. Paleoclimate model simulations in contrast to future projections, have the advantage, that there

are proxy data available, which help to validate the model's response to any changes in the forcing. Proxies help reducing the uncertainties, when modelling a climate state in extreme circumstances. One of the best examples of past warm periods is the Early Eocene Climatic Optimum (EECO, ~56-48 Myr ago). It is the period of greatest sustained (> 1 Myr) warmth in the last 65 million years (Lunt et al., 2017) ,when CO_2 concentrations are estimated to have fallen between 1170 and 2490 ppm (Anagnostou et al., 2020) and the estimated global mean surface temperatures reached 27.0 °C (23.2 to 29.7 °C), approximately 10 to 16 °C warmer than preindustrial climate (Inglis et al., 2020). It has been shown (Evans et al., 2018), that the meridional temperature gradient was much weaker in the Eocene's warm climate than at present, thus indicating strong polar amplification, which is a challenge to capture for most climate models. There has been a community effort in creating a framework for the intermodel comparison of Paleocene-Eocene simulations (Lunt et al., 2017) and also to coordinate the methodology of a proxy data compilation focusing on temperature and CO_2 concentrations from this period (Hollis et al., 2019). This coordinated effort is the Deep Time Model Intercomparison Project (DeepMIP), and the time intervals its focusing on are the latest Paleocene (pre-PETM), Paleocene–Eocene thermal maximum (PETM) and early Eocene climatic optimum (EECO). In DeepMIP, the atmospheric CO_2 concentrations and other boundary conditions, such as the paleogeography, orbital configurations, solar constant, vegetation, and lack of continental ice sheets were uniformly defined. Eight modelling groups participated in performing paleo simulations, with the agreed boundary conditions. Some models are closer to the proxy records than others, but all simulations indicate a warmer, than present day global mean temperature and a smaller, than present day meridional SST gradient. The Community Earth System Model (CESM), the Geophysical Fluid Dynamics Laboratory model (GFDL) and the Norwegian Earth System Model (NorESM) perform well in simulating the global mean temperature and meridional SST gradient at CO_2 levels, which are also in the proxy indicated range (Lunt et al., 2021). The closest agreement with proxy data is found for simulations at 6x times the preindustrial CO_2 concentration, which also aligns with the best-estimate of CO_2 signal from proxy data. In terms of simulating the lowest meridional temperature gradient the most successful simulation is from CESM (Lunt et al., 2021).

Several studies have investigated the EECO's heat transport with the intention to explain its low temperature gradient. Increased heat transport, especially increased ocean transport have been suggested to be the mechanism responsible for the low meridional gradient (Barron, 1987; Sloan et al., 1995). It has been estimated that 30% or even greater increase in poleward heat transport, than at present is needed to achieve the low temperature gradient of Eocene (Huber & Nof, 2006; Sloan et al., 1995). This is problematic, since we do not know any acceptable mechanism to realize such a large transport change, neither is it something any respective modelling study would have indicated. The Eocene meridional heat transport have been studied with coupled global circulation models (Heinemann et al., 2009; Huber & Sloan, 2001), and their results support the notion that not the increased oceanic heat transport is the responsible mechanism for the low meridional temperature gradient.

In our work we focus on the changes in the different atmospheric transport processes in the EECO, to better understand the atmospheric large scale circulation pattern of this warm climate. Moreover, we separate these changes depending on their underlying causes, namely if they are driven by the CO_2 increase or the non-CO_2 forcing of the paleo simulations. We compare the results of five different models from the DeepMIP ensemble. Dividing the changes into non-CO_2 and CO_2 forcing helps us to also assess the relevance of the results for future

164 climate scenarios, where the CO_2-driven processes become more relevant than any changes in
165 topography. Our study aims to answer the following questions:

166 • Can the DeepMIP model ensemble capture the characteristics of transport processes in
167 the preindustrial control (PI) simulations?

168 • What are the impacts of changes of non-CO_2 constraints (paleogeography, vegetation, no
169 continental ice sheet) on the different atmospheric transport processes?

170 • What are the impacts of CO_2 concentration increase on the atmospheric transport
171 processes in the 3x and 6x CO_2 EECO simulations?

172 • How does the overall change (non-CO_2 and CO_2 constraints) between the preindustrial
173 control and EECO simulations look like? Which physical transport processes are affected
174 the most?

175 The paper is structured as follows, in section 2 we briefly introduce the DeepMIP
176 experimental design, the selected models and reanalysis, and we explain the methods used in the
177 analysis. Then the results section shows the transport changes due to the non-CO_2 and the CO_2
178 constraints, first individually and then their combined effect on changes between past and present
179 climates. Then section 4 discusses the three large scale circulation patterns, which are affected by
180 either one or both of the CO_2 and non-CO_2 constraints. In section 5 we summarize our findings
181 and conclude.

182 **2 Data and Methods**

183 In this study we analyze climate model simulations from DeepMIP simulations. We
184 further include present day data from the ERA5 reanalysis to compare it with the respective
185 preindustrial simulations of the DeepMIP models.

186 2.1 Experimental design

187 The experimental design and the different models included in DeepMIP are described in
188 Lunt et al. (2017, 2021), here we only introduce them briefly. DeepMIP was conducted to offer a
189 consistent framework for climate model simulations of three warm periods in the latest
190 Paleocene and early Eocene (~ 55 to ~ 50 Ma), which are the Early Eocene Climatic Optimum
191 (EECO), the Paleocene–Eocene Thermal Maximum (PETM) and the period just before the
192 PETM (pre-PETM). These time periods of Earth's climate are characterized by high atmospheric
193 CO2 concentrations estimated to be between 800 and 3160 ppm (Anagnostou et al., 2020), which
194 means at least 3x higher concentrations than the preindustrial value (280 ppm) and almost 12x
195 more at its highest. The concentrations during the EECO, which is the longest of the three, is
196 estimated to fall between 1170 and 2490 ppm. This is around 4x and 9x the preindustrial
197 concentration level. Many DeepMIP groups performed multiple experiments at various CO_2
198 levels, for example at 1x, 3x, 6x or 9x the preindustrial CO_2 concentration, to capture this
199 uncertainty. Apart from the atmospheric CO_2 concentrations other boundary conditions, such as
200 the paleogeography, orbital configurations, solar constant, vegetation, continental ice sheets and
201 aerosols, are needed to be defined to set up a deep-time simulation. The paleogeography
202 represents the Ypresian stage of the Eocene, where the most notable differences to today's
203 geography are the lack of the Himalaya, the lack of the enclosed Mediterranean basin, the proto-
204 Paratethys and the Siberian Sea and a narrower Atlantic basin. The digital reconstruction from

Herold et al. (2014) is used for the paleogeography, vegetation, and river routing. The orbital configuration is set to the modern values, because it represents a forcing close to the long-term average (Lunt et al., 2017). Both the solar constant, and non-CO_2 greenhouse gas concentrations are set to preindustrial values, to find a middle ground between the uncertainty on the increased radiative forcing associated with enhanced non-CO_2 greenhouse gases and the decrease in radiative forcing via a reduced solar constant (Lunt et al., 2017). One additional important initial constraint is that there are no continental ice sheets in the Eocene simulations. Initial condition for ocean temperature and salinity are given in Lunt et al. (2017) but each modeling group followed their individual approach based on their previous paleo simulations or experiences with model instabilities.

To accept a model simulation as the representation of the paleoclimate of EECO, PETM, or pre-PETM it needs to be in (or close to) equilibrium. To assure this, three criteria are defined, the first is regarding the length of the simulation (more than 1000 years) the second considers the energy balance of the models (less than 0.3 W m−2 net radiation imbalance at the top of the atmosphere or similar imbalance to that of the preindustrial control), and last is the test if the ocean have reached its equilibrium state (sea-surface temperature trend is less than 0.1°C per century in the global mean). These latter two shall be based on the final 100 years of the simulation. Most of the simulations fulfill these conditions, and those which are not, only overstep the thresholds slightly, thus Lunt et al. (2021) concluded them to be sufficiently equilibrated.

Table 1

List of models used in this study from the DeepMIP ensemble.

Model (short name)	Experiments	Length of simulations (years)	Atmospheric resolutions (lat x lon)
CESM (CESM1.2_CAM5)	piControl 1x,3x,6x	2000	1.9° x 2.5°
COSMOS (COSMOS-landveg_r2413)	piControl 1x,3x	9500	3.75° x 3.75°
GFDL (GFDL_CM2.1)	piControl 1x,3x,6x	6000	3° x 3.75°
HadCM3 (HadCM3B_M2.1aN)	piControl 1x,3x	7800	3.75° x 2.5°
MIROC (MIROC4m)	piControl 1x,3x	5000	2.79° x 2.81°

2.2 Models

In total 8 models participated in DeepMIP from which we selected 5, depending on the available experiment types. In our study we focus on the CO_2 and non-CO_2 effects, thus we

needed from all models a preindustrial control simulation, a 1x CO2 Eocene simulation, and also at least one Eocene simulation with a higher CO_2 concentration. The three models, which we did not include in our study (INMCM, IPSL, NorESM), are left out because there was no available 1x CO2 simulation from them. We have chosen 3x and 6x CO2 concentration simulations, where they were available (see Table1). These concentrations, represent the pre-PETM and the EECO/PETM conditions respectively. All models are coupled ocean-atmosphere models. The selected simulations are summarized in Table 1. An overview of each model is listed below, while the more elaborate description of the simulations and models are found in Lunt et al. (2021) and in the corresponding papers.

CESM stands for the Community Earth System Model version 1.2, it consists of the Community Atmosphere Model 5.3 (CAM), the Community Land Model 4.0 (CLM), the Parallel Ocean Program 2 (POP), the Los Alamos sea ice model 4 (CICE), the River Transport Model (RTM), and a coupler connecting them (Hurrell et al., 2013). The atmospheric part of the coupled system has 30 hybrid sigma-pressure levels and a horizontal resolution of 1.9° × 2.5° (latitude × longitude).The ocean and sea ice model use a nominal 1°x1° displaced pole Greenland grid with 60 vertical levels in the ocean. Some modifications were needed to make the Earth system model applicable for a paleoclimate simulation with a high CO2 level applicable. These effected the radiation parametrization, and the marginal sea balancing scheme. The ocean was initialized from a previous PETM simulation (Kiehl & Shields, 2013) without any sea ice. The simulations have been integrated for 2000 model years, except the 1xCO2 simulation, which has been integrated for 2600 model years.

COSMOS is developed at the Max Planck Institute for Meteorology and uses the atmospheric general circulation model ECHAM5 (Roeckner et al., 2003) and the Max-Planck-Institute for Meteorology Ocean Model (MPIOM) (Marsland et al., 2003) for the the ocean and sea ice components. The atmospheric part has 19 vertical hybrid sigma-pressure levels and a horizontal resolution approximately 3.75° × 3.75°. The ocean and sea ice dynamics are calculated on a bipolar curvilinear model grid with formal resolution of 3.0° × 1.8° (longitude × latitude) and 40 unequal vertical levels. COSMOS' performance in paleoclimate studies is described in Stepanek and Lohmann, (2012). The ocean was initialized with uniformly horizontal and vertical temperatures of 10 °C in the 3×CO2 concentration simulation and then the simulations with 1 × and 4× CO2 concentrations were restarted from 3×CO2 after 1000 years. The simulations were started with transient orbital configurations and were run for model year 8000, then they were run with preindustrial orbital parameters for the last 1500 years.

GFDL means the Geophysical Fluid Dynamics Laboratory (GFDL) CM2.1 model (Delworth et al., 2006), with modifications to the late Eocene (Hutchinson et al., 2018, 2019). The CM2.1 consists of Atmosphere Model 2, Land Model 2, the Sea Ice Simulator 1. The ocean is calculated by the modular ocean model (MOM) version 5.1.0. The atmosphere has 24 vertical levels and a horizontal resolution of 3° × 3.75°. The ocean and sea ice components are calculated over 50 vertical levels with the horizontal resolution of 1◦ × 1.5◦ (latitude × longitude), and a tripolar grid is used as in Hutchinson et al. (2018). Due to the paleogeography some manual adjustments were made in the ocean grid. The ocean temperature was initiated from idealized conditions, similar to those outlined in Lunt et al. (2017). The simulations were run for a total of 6000 years. During the initial 2000 years, two adjustments were performed on the ocean temperature to accelerate the approach to equilibrium. This approach led to instabilities

at 6xCO2 level, this simulation was instead initialized using a globally uniform temperature of 19.32 °C and was run continuously for 6000 years.

HadCM3 is the abbreviation of the Hadley Centre Climate Model (Valdes et al., 2017). The atmosphere has 19 vertical levels and a horizontal resolution of 3.7° × 2.5° , while the ocean is calculated on a 1.25° × 1.25° grid over 20 vertical levels. A few changes were necessary to adapt the model to the deep-time simulations, such as a salinity flux correction, prognostic 1D ozone scheme instead the fixed vertical profile, and also the disabling of modern-day specific parametrizations, e.g., in the Mediterranean and the Hudson Bay. The ocean was initialized from the final state of Eocene model simulations using lower resolution in the ocean, HadCM3L. The HadCM3L simulations were initialized from a similar idealized temperature and salinity state as described in Lunt et al., (2017). HadCM3 simulations were started from the respective HadCM3L integrations after 4400 to 4900 years of spin up and run for a further 2950 years.

MIROC stands for Model for Interdisciplinary Research on Climate (Chan & Abe-Ouchi, 2020). The land surface model is the Minimal Advanced Treatments of Surface Interaction and Runoff (MATSIRO) (Takata et al., 2003). The ocean component is the version 3.4 of the CCSR (Center for Climate System Research) Ocean Component Model (COCO) (Hasumi, 2000). The atmosphere has 20 vertical sigma levels and a horizontal resolution of approximately 2.79° x 2.81° (latitude x longitude).The ocean has 44 levels and a horizontal resolution is set to 256 × 196 (longitude × latitude), with a higher resolution in the tropics. The atmosphere is initialized from a previous experiment without ice sheets and with a × 2 CO2 concentration. The ocean is initialized based on previous MIROC paleoclimate experiments and on the recommendations from Lunt et al. (2017). For the experiments the model was run for 5000 model years.

2.3 Reanalysis

We use the atmospheric reanalysis ERA5 (Hans Hersbach et al., 2020) to evaluate the DeepMIP ensembles performance for the preindustrial control simulation. ERA5 is a comprehensive reanalysis from Copernicus Climate Change Service (C3S) produced by ECMWF and it is based on the Integrated Forecasting System (IFS) Cy41r2 which was operational in 2016. In our study we used monthly averaged data on pressure levels and on single levels (H. Hersbach et al., 2019b, 2019a) from the time period 1991-2020 on a horizontal resolution of approximately 0.25°x0.25°.

2.4 Partitioning the meridional heat transport

In our study we analyze the total meridional heat transport, and focus on its components, in the atmosphere. We follow the method described in Donohoe et al. (2020). First the MHT is partitioned between the ocean and the atmosphere

$$MHT = OHT + AHT\,, \qquad (1)$$

and the atmospheric transport is further partitioned into contributions from meridional overturning circulation (MOC), stationary eddies (SE) and transient eddies (TE)

$$AHT = MOC + SE + TE. \qquad (2)$$

Furthermore, all parts of Eq. (2) are divided into dry and moist energy transport (Eq. 3), where the moist part consists the transport of energy via latent heat and the dry part consists the transport of potential energy and sensible heat.

$$AHT = AHT_{moist} + AHT_{dry}$$

$$MOC = MOC_{moist} + MOC_{dry}$$

$$SE = SE_{moist} + SE_{dry}$$

$$TE = TE_{moist} + TE_{dry} \quad (3)$$

The total meridional heat transport at a latitude circle can be calculated with dynamic and energetic approaches, where in the energetic approach the MHT is balanced by the spatial integral of the net radiative deficit at the top of the atmosphere (TOA) and in the dynamic approach MHT is the vertically and zonally integrated net transport of energy. Here we use the energetic approach to calculate MHT (Eq.4)

$$MHT(\Phi) = 2\pi a^2 \int_{-\frac{\pi}{2}}^{\Phi} \cos\Phi' \, [ASR(\Phi') - OLR(\Phi')] d\Phi', \quad (4)$$

where ϕ is the latitude circle, a is the radius of the Earth, ASR is the absorbed solar radiation, OLR is the outgoing longwave radiation. The boundary condition is that the transport has to be zero at the pole, because non-zero values have no physical meaning. To fulfill the boundary conditions at both poles, we need to balance the global budget. For this we assume that the imbalance is spatially uniform, thus the area-weighted global average energy imbalance is subtracted at all latitudes before calculating the integral in Eq. (4).

OHT can also be calculated with the energy approach from the surface heat fluxes (SHF) (Eq. 5)

$$OHT(\Phi) = 2\pi a^2 \int_{-\frac{\pi}{2}}^{\Phi} \cos\Phi' \, [SHF(\Phi')] d\Phi', \quad (5)$$

where SHF is positive downward. The above equation is true with the assumption that the ocean is in equilibrium, so the heat storage is negligible. If the ocean is not in an equilibrium state, then Eq. (5) represents the implied OHT, which is the sum of OHT and the spatial integral of the tendency of ocean heat content. The DeepMIP simulations have been required to fulfill different criteria to prove that they reached the equilibrium state. The criteria considered the length of the simulations, the radiation imbalance at the TOA, and the ocean's equilibrium state. All of the included simulations satisfy at least two of the three criteria, with the only exception of CESM at 3xCO_2, which is still close to both missed criteria, thus all, here considered simulations, have been accepted to be sufficiently equilibrated (Lunt et al., 2021). We consider Eq.(5) defining OHT and that balancing the global radiative budget at the TOA does not largely affect largely the calculation of MHT.

After calculating MHT and OHT given Eq. (1) AHT is known as the residual. The direct dynamical calculation of AHT is formulated via the vertically and zonally integrated meridional

transport of moist static energy (MSE):

$$MSE = c_p T + Lq + gZ$$

$$AHT(\Phi) = \frac{2\pi a \cos\Phi}{g} \int_0^{P_s} [\bar{V}]\,[\overline{MSE}] + [V^* MSE^*] + \left[\overline{V'^* MSE'^*}\right] + \overline{[V]'[MSE]}' dp, \quad (6)$$

where cp is the specific heat capacity of air at constant pressure, T is temperature, L is the latent heat of vaporization of water, q is the specific humidity, g is the acceleration of gravity, Z is the geopotential height, P_s the surface pressure, V is the meridional velocity. The square brackets [x] denote zonal averages, the overbars $\bar{x}$ denote time averages (monthly means), x* denote zonal anomalies, and x' means time anomalies. In Eq. (6) the first term defines the energy transported via MOC the second is SE, the third is TE, and the last one has been referred as the transient overturning circulation (TOC) (Marshall et al., 2014), which is two orders of magnitudes smaller than MOC at the tropics and the eddy terms at midlatitudes. Thus, we do not try to consider TOC on its own, but handle it together with TE. Note that the calculation of TE and TOC would require high temporal resolution data, which is not available for the DeepMIP simulations, thus we cannot calculate AHT only from Eq. (6), hence we use the residual method via Eq. (1). Nevertheless, the transport via MOC and SE is calculated from Eq. (6) with monthly mean data. The remaining atmospheric transport, which we refer to as TE, is again defined with a residual method. This TE calculation, has been shown to be successful in calculating the partitions from monthly mean data with good accuracy (Donohoe et al., 2020).

Regarding the moist and dry partitioning for AHT we define AHT_{moist} as the latent heat transport at a given latitude, which is the integral of evaporation (E) minus precipitation (P) multiplied by the latent heat of vaporization:

$$AHT_{moist}(\Phi) = 2\pi a^2 \int_{-\frac{\pi}{2}}^{\Phi} \cos\Phi' \{L[E(\Phi') - P(\Phi')]\} d\Phi' \quad . \quad (7)$$

The dry contribution to AHT is then calculated by subtracting the moist part from the total (Eq. 3). The moist and the dry parts of MOC an SE are calculated via Eq.(6), but MSE has been split into dry, the sensible heat and potential energy (cpT+gZ) and moist part, the latent heat (qL) (Donohoe et al., 2020). The moist and dry contributors to TE can be calculated via the residual method, with the use of Eq. (3) and:

$$AHT_{moist} = MOC_{moist} + SE_{moist} + TE_{moist}.$$

2.5 Meridional Streamfunction

There are several metrics to quantitively analyze the Hadley cell, its edge and its circulation strenght. We choose to use the average meridional streamfunction Ψ (Xian et al., 2021) to quantify its intensity, which is defined as :

$$\Psi(p, \Phi) = \frac{2\pi a \cos\Phi}{g} \int_{P_s}^{0} [v] dp \ .$$

A stronger streamfunction means a stronger Hadley cell circulation.

2.6 Monsoon Area

The monsoon climate is characterized by seasonal reversal of prevailing surface winds which results in a rainy summer and dry winter. To assess the geological area where monsoon was probably present in the EECO, we use a simple monsoon definition, which is also used in the 6th Assessment Report of IPCC (IPCC, 2021). The global monsoon is defined as the area, where the local annual range of precipitation exceeds 2.5 mm per day (Kitoh et al., 2013). The annual range is defined by the local summer- minus-winter precipitation, i.e. MJJAS minus NDJFM in the Northern Hemisphere and NDJFM minus MJJAS in the Southern Hemisphere. The 2.5 mm per day threshold is defined based on current conditions, which might not hold so well in a warmer world, nevertheless we accept it for our rough estimations. A more detailed analysis of the monsoon systems is to follow this study, where not just such simple indices will be used.

3 Results

3.1 Preindustrial control simulation

We start our analysis by evaluating the selected models' representation of present day climate, more precisely the climate of the preindustrial period. To assess the models' results we compare them to transport values calculated from the ERA5 reanalysis from 1991-2020. Note that this comparison is not entirely fair since the models and the reanalysis represent two different climate periods approximately 150 years apart, and in this one and a half century the climate constraints, especially the CO_2 concentration have changed. Nevertheless, both models and reanalysis represent a climate with current topography, continental ice sheets and relatively similar meridional temperature gradient, when compared to our knowledge of EECO's climate. Thus, we accept these discrepancies and focus on the structure of the transport processes, and not on the quantitative amounts.

The meridional heat transport and its partitions calculated from the DeepMIP models and the ERA5 reanalysis are shown in Figure 1. Overall, there is good agreement between the mean of the model ensemble and the reanalysis. The values and distributions of the MHT and its components fit well also to previous studies which are based on observations and reanalysis (Donohoe et al., 2020; Masuda, 1988).

MHT reaches maximum of above 5 PW at around 40° both South and North. The ocean transports more heat than the atmosphere in a narrow tropical belt (0-10 °N), outside of which the atmospheric heat transport dominates (Figure 1a). The reanalysis is within the spread of the DeepMIP ensemble. The ensemble mean fits the reanalysis better over the southern hemisphere than over the northern, where the models transport more via the atmosphere and less via the ocean. These two compensate each other resulting in a good fit for the total MHT.

The atmospheric transport partitioned into latent heat and dry static energy transport (Figure 1c) shows that the two have similar order of magnitude, but the dry static energy transport is at all latitudes poleward, while the latent heat transport is equatorward in the tropics and poleward at the rest of the latitudes.

Partitioning of the atmospheric heat transport into meridional overturning circulation,

stationary, and transient eddies shows that transport is (a) mainly in transient eddies in the midlatitudes, i.e. in extratropical cyclones, and (b) dominantly by meridional overturning circulation, i.e., by the Hadley cells, in the tropics (Figure 1b). The tropical belt is where some differences between the models and the reanalysis arises, namely over the Southern Hemisphere the reanalysis shows more northward transport via meridional overturning circulation, MOC, and more southward transport via transient eddies, TE. Since these two mechanisms act in the different direction, the AHT does not show large differences between the reanalysis and the ensemble mean. The separation of the MOC into its dry and moist parts (Figure 1e) reflects the poleward transport of potential and sensible heat in the upper part of the Hadley cell and the equatorward latent heat transport in the lower part of the Hadley cell. The transport of the two parts do not balance out each other resulting in a net poleward energy transport. Stationary eddies show importance in the poleward latent heat transport around 30° in both hemispheres, representing the monsoon systems (Figure 1d). Stationary eddies also transport dry static energy to the northern midlatitudes, mainly during winter, representing planetary waves (Masuda, 1988). Extratropical cyclones transport heat in both, the moist and dry form (Figure 1b and f).

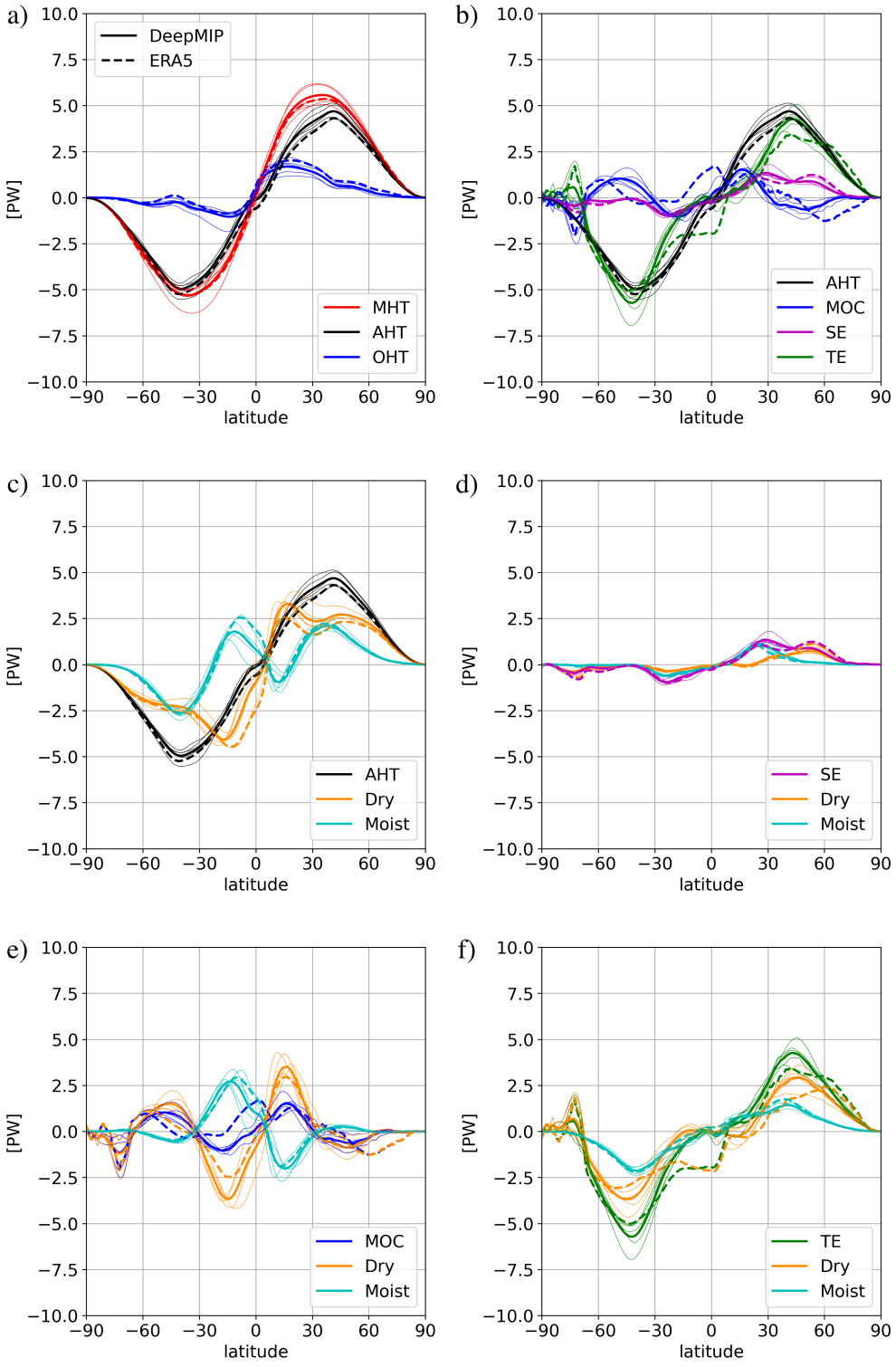

441

442 **Figure 1**. Annual meridional heat transport and its different parts in the preindustrial control
443 simulations of the 5 DeepMIP ensemble members and the ERA5 reanalysis. Bold lines
444 representing the ensemble mean thin lines representing each model and dashed lines are
445 calculated from ERA5 (1991-2020) reanalysis. The partitions of MHT are (a) Meridional Heat
446 Transport, divided between atmospheric (AHT) and oceanic (OHT) part, (b) atmospheric

transport divided into Meridional Overturning Circulation (MOC), Stationary Eddies (SE) and Transient Eddies (TE), (c) atmospheric transport divided to dry and moist parts, (d) atmospheric transport via SE and its dry and moist parts, (e) atmospheric transport via MOC and its dry and moist parts, and (f) atmospheric transport via TE and its dry and moist parts.

3.2 Effect of the Non-CO_2 forcing on the Eocene MHT

The Eocene 1xCO_2 simulations, i.e., with non-CO_2 forcing because of changes in paleogeography and vegetation or the lack of continental ice sheets, are 3-5 °C warmer than the preindustrial simulations (Lunt et al., 2021). Figure 2 shows the MHT differences between the Eocene 1xCO_2 and the preindustrial control simulation. There is more southward MHT in the 1xCO_2 simulation than in the preindustrial one, which is mainly due to an increase in the oceanic southward heat transport (Figure 2a). This results in smaller poleward MHT in the Northern Hemisphere but larger in the Southern Hemisphere during the Eocene. In other words, due to the Eocene boundary conditions the atmospheric poleward transport increases and the ocean transport decreases in the Northern Hemisphere and vice versa in the Southern Hemisphere.

The change in atmospheric dry and moist transport is also asymmetric. North from the Tropic of Cancer (30°N) more latent heat is transported northward and south from it more latent heat is transported southward in the Eocene than in the preindustrial climate. The dry static heat transport changes show the opposite sign. When taking into consideration the direction of transport (see Figure 1c), this means that over the Northern Hemisphere there is more moisture transport equatorward in the tropics and more poleward transport at midlatitudes, while the dry static energy transport compensates these changes, with more poleward transport at the tropics and less at higher latitudes (Figure 2c). On the other hand, over the Southern Hemisphere the tropical equatorward latent heat transport decreases and the extratropical poleward latent heat transport increases. The poleward dry static energy transport decreases at all southern latitudes. These together lead to a net increase (decrease) in atmospheric poleward transport in the Northern (Southern) Hemisphere, which as mentioned above is overcompensated by the ocean. An increase in poleward latent heat transport also has an important role in polar amplification.

The most prominent atmospheric change is the increased heat transport by transient eddies between 30°N-60°N and 60°S-90°S (Figure 2b). These represent heat transport by extratropical cyclones, thus cyclones are more frequent and/or more intense in the Eocene simulations. To quantify the number of cyclones and their features, more frequent than monthly model output would be needed. The increased transient eddies transport is mostly compensated by stationary eddies and meridional overturning circulation transports (Figure 2b). There is also a decrease in the northern hemisphere monsoonal transport (Figure 2d). The Hadley circulation also shows an asymmetric shift, with more energy being overturned in the northern cell, and less in the southern one, while the net poleward MOC energy transport stays close to the control simulation (Figure 2e).

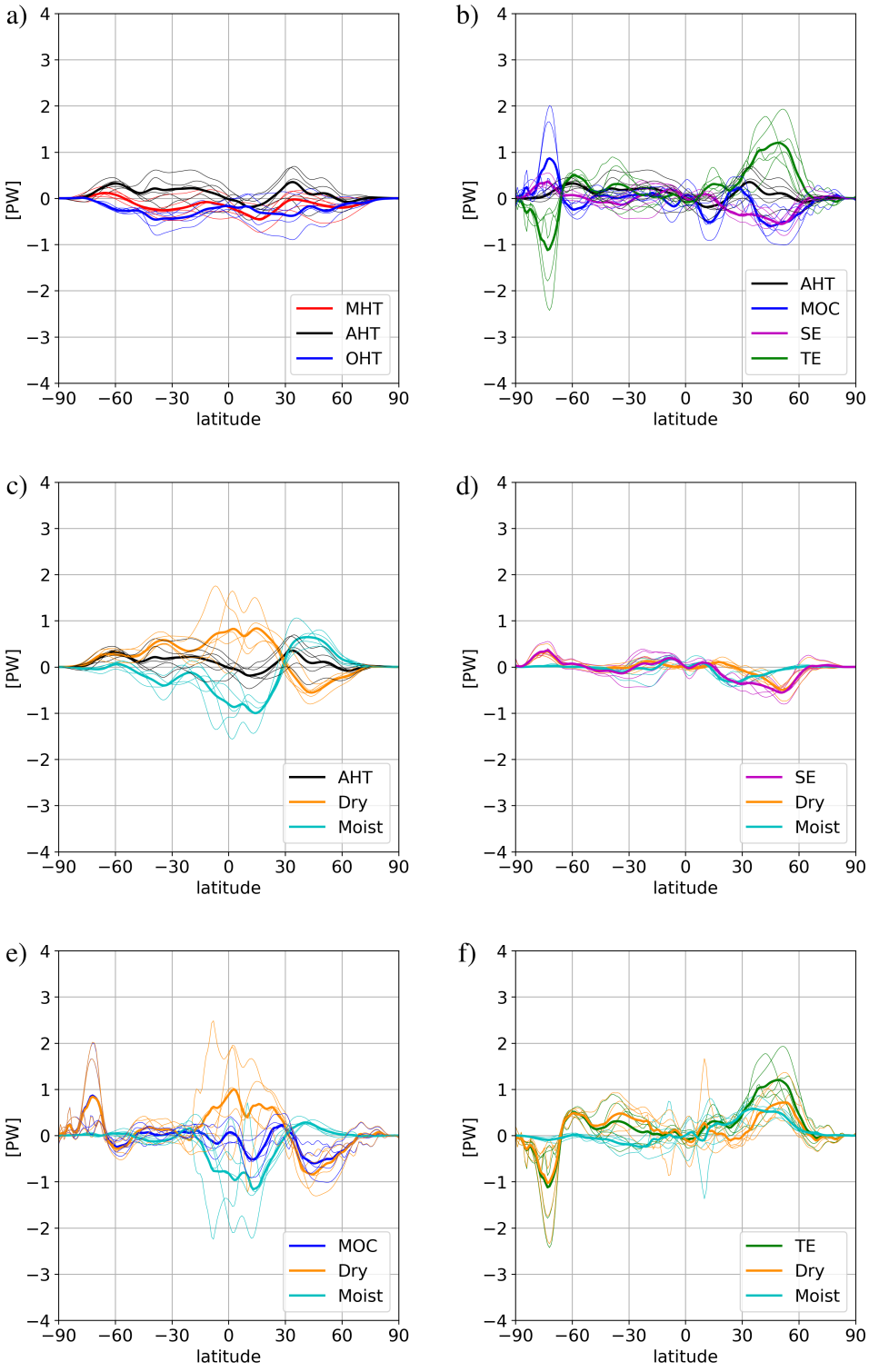

Figure 2. Meridional Heat Transport and its parts, same as Figure 1, but showing the differences between the 1xCO_2 Eocene and the preindustrial control simulations.

3.3 Effect of the CO_2 forcing on the Eocene MHT

The effect of higher CO_2 concentrations on early Eocene transport processes is studied by quantifying the changes between the $3xCO_2$ and $6xCO_2$ simulations relative to the $1xCO_2$ simulation (Figure 3 and 4). We compare the $6xCO_2$ simulation also to the $1xCO_2$ one to display the intensification of the signal due to CO_2 rise. Our choosen DeepMIP ensemble has five models available with $3xCO_2$ simulations and only two with $6xCO_2$ simulations (CESM & GFDL, see Tab. 1). The two latter simulations are shown to be the most successful in representing the global mean surface temperature, global mean SST and global meridional SST gradient when compared to proxy data (Lunt et al., 2021) and thus we trust this small ensemble is still representative.

When comparing the changes relative to the equator, we see mostly symmetric changes, thus the effect of CO_2 rise is global and influences both hemispheres in a similar way. For the $3xCO_2$ simulation we find an increase in poleward MHT compared to the $1xCO_2$ simulation, which mainly results from the atmosphere (Figure 3a), while at the $6xCO_2$ simulation the MHT is fluctuating around zero (Figure 4a). In the latter case anomalies in the atmospheric and ocean heat transport counteract one another, i.e., the Bjerknes compensation is present. The differences between the two figures, and hence CO_2 concentrations, can also arise from the different set of models used for the ensemble mean. Especially, since GFDL presents a non-linear behavior, and from $4xCO_2$ to $6xCO_2$ concentration a slight decrease in the full MHT is found over the Northern Hemisphere. Its magnitude is smaller than the CESM signal, thus the ensemble mean still indicates a positive poleward transport change. Nevertheless, both at $3xCO_2$ and $6xCO_2$ concentration, the poleward atmospheric heat transport increases and ocean's heat transport decreases or stays close to the $1xCO_2$ value in the ensemble mean. Polar amplification is also represented via the increased latent heat transport from the subtropics towards the poles, compensated by the dry static heat transport (Figure 3c and 4c). Regarding the different physical processes in the atmosphere, we see similar changes in both $3xCO_2$ and $6xCO_2$ simulations. (Figure 3b and 4b). At the tropics the change in the net meridional overturning circulation transport is close to zero, but the dry static and latent heat energy transport of the Hadley cell increases more so at the northern cell than at the south (Figure 3e and 4e). The subtropics, are mostly defined by the increased poleward transport of moist stationary eddies, namely the transport of the monsoon systems, more in the 6xCO2 than in the $3xCO_2$ simulation (Figure 3d and 4d). At midlatitudes the poleward transport of transient eddies increases slightly, especially in the $6xCO_2$ simulations (Figure 4f), but the magnitude of change is smaller than, what the non-CO_2 constraints caused in the $1xCO_2$ simulations (see Figure 2f).

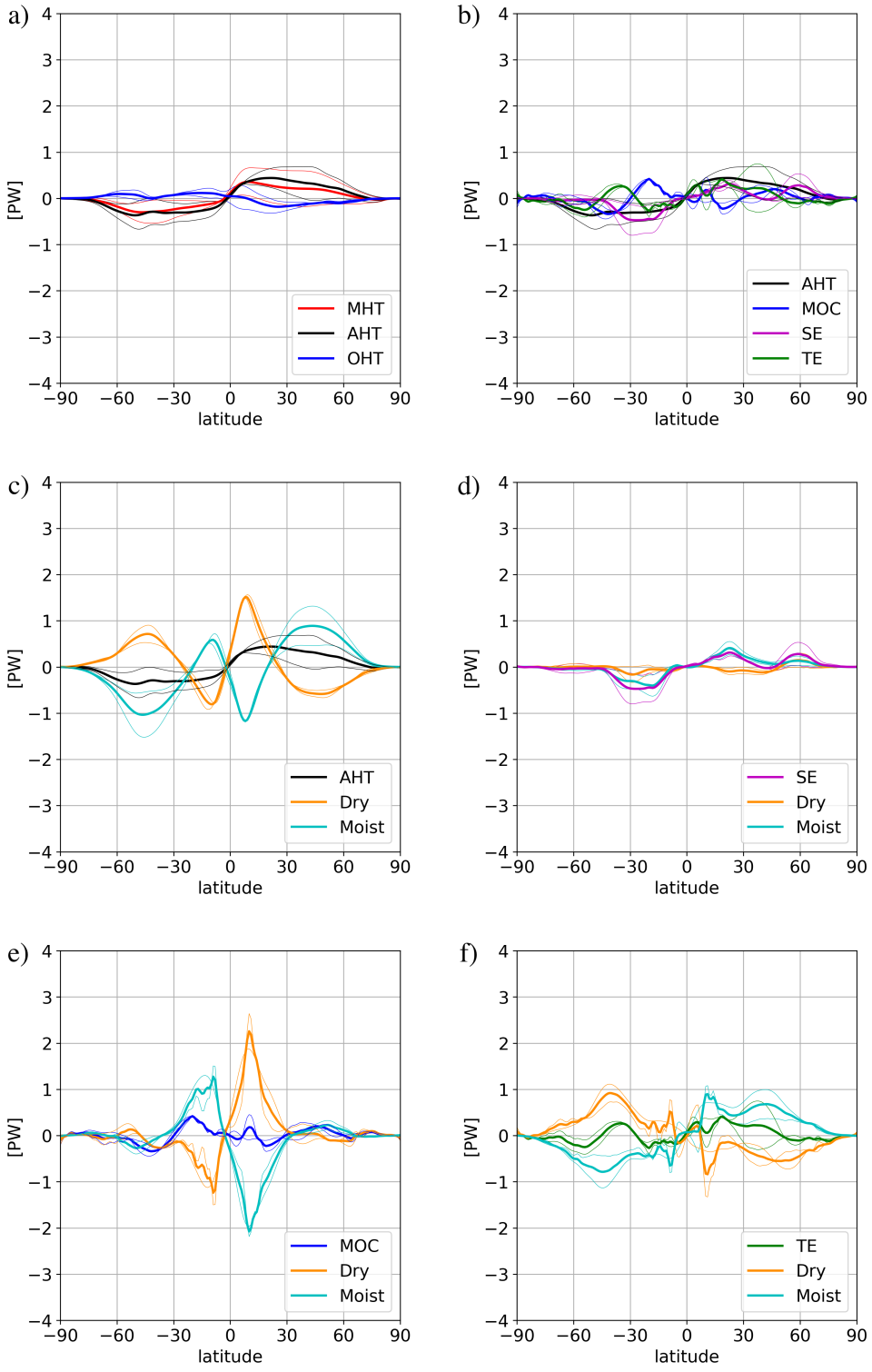

Figure 3. Meridional Heat Transport and its parts, same as Figure 2, but showing the differences between the $3xCO_2$ and the $1xCO_2$ paleo simulation.

526

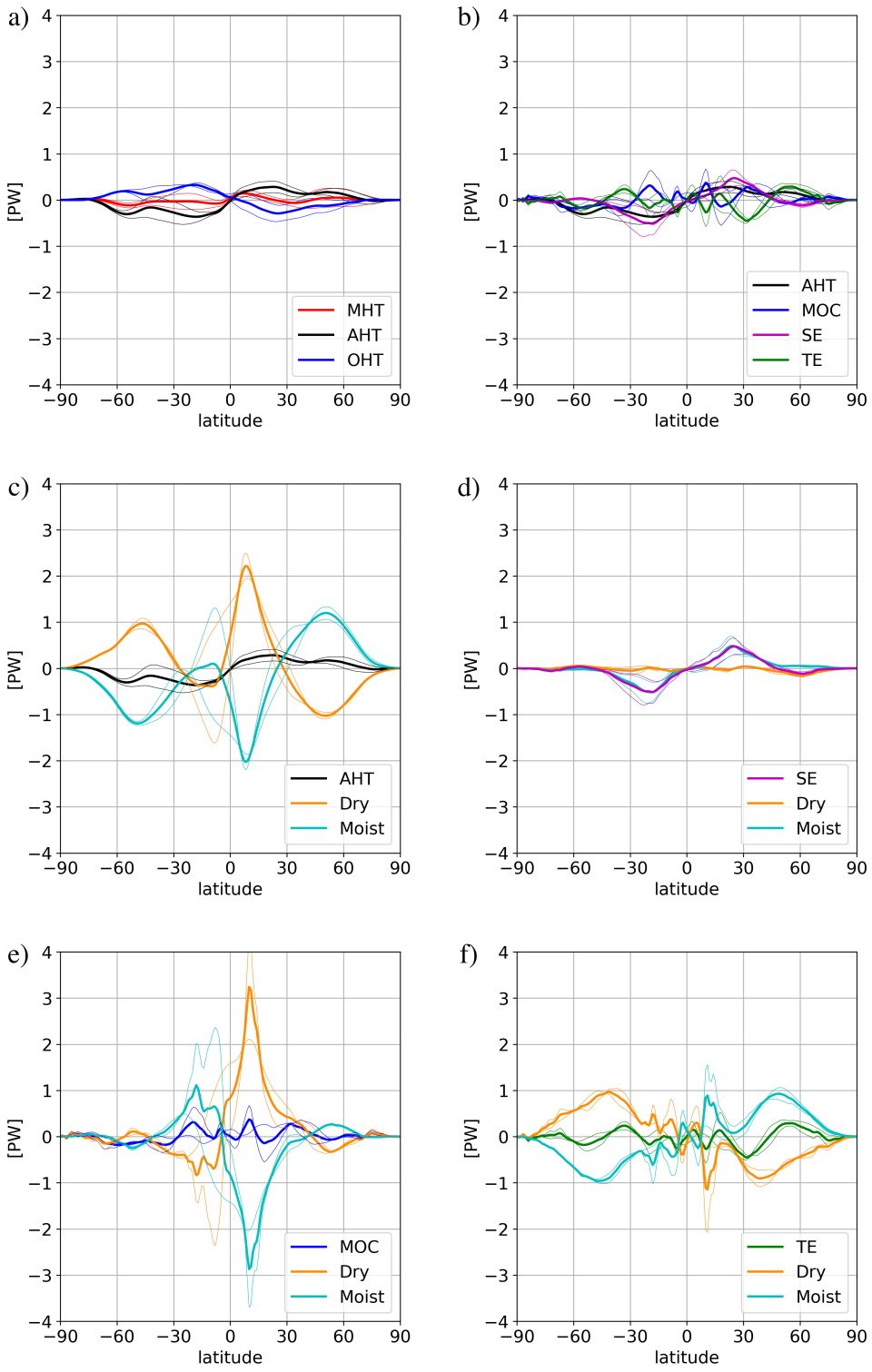

527

528 **Figure 4**. Meridional Heat Transport and its parts, same as Figure 3, but showing the
529 differences between the 6xCO_2 and the 1xCO_2 paleo simulation. The ensemble here consists only
530 two models: CESM, GFDL.

3.4 Effect of the total forcing on the Eocene MHT

Finally, we investigate the overall heat transport changes between the simulated preindustrial and most-likely Eocene climate states. This is important as it is the relevant change when comparing Eocene proxy data to present day conditions, and because the individual changes due to the CO_2 and the non-CO_2 constrains are potentially nonlinear and can counteract each other.

In total meridional heat transport, we see more changes compared to the present day climate in the Northern Hemisphere, where the atmosphere transports more energy while the ocean compensates this with less transport (Figure 5a). There is an increase of latent heat transport toward the polar regions at both hemispheres in the EECO climate, which is compensated by the decrease in dry static energy transport at the midlatitudes (Figure 5c). In the tropics the net transport via meridional overturning circulation stays close to the preindustrial values, but the dry (poleward) and moist (equatorward) energy transport increases in the Hadley cell, especially in the northern cell (Figure 5e). In the southern subtropics the EECO simulations show slightly more latent heat transport via stationary eddies (Figure 5d). This means that the monsoon systems in the Southern Hemisphere transported more energy during the EECO. Nevertheless, it has been shown in the previous two subsections that the monsoon in the Northern Hemisphere also changed, but with opposite signs due to the respective CO_2 and non-CO_2 forcings. Thus, the overall monsoonal transport changes in the Northern Hemisphere are small. At the midlatitudes, especially in the Northern Hemisphere more energy is transported via transient eddies (cyclones) during the Eocene, which is again compensated by less transport via stationary eddies (Figure 5b,d,and e). In the Southern Hemisphere we find slightly less transient eddy transport in the EECO than in the preindustrial simulations.

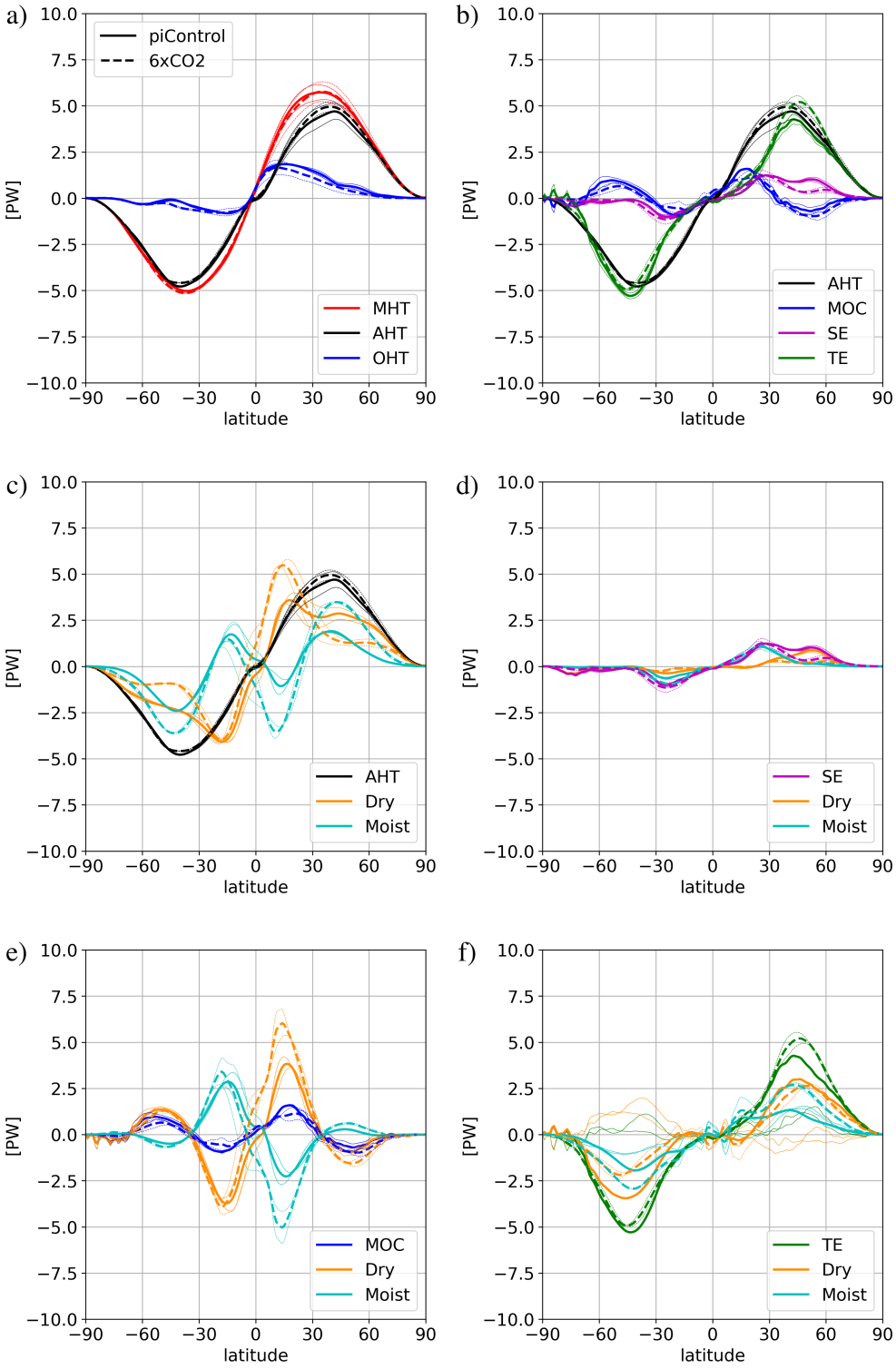

Figure 5. Meridional Heat Transport and its parts, same as Figure 1, but showing the preindustrial control (solid lines) and 6xCO2 (dashed lines) simulation results. The included models are: CESM, GFDL.

4 Discussion

The analysis of the different transport processes identified those large scale circulation patterns, which are either effected by the changes in the paleo set up or by the changes in the CO_2 concentration. These, heading from the tropics to the pole, are the Hadley cell, the monsoon and the mid-latitude cyclones. In this section we discuss the changes in these large scale patterns in more detail.

4.1 Hadley Cell

We found that due to both the CO_2 and non-CO_2 constraints more dry static energy and latent heat is turned around by the Hadley cells. Since all these simulations have a generally warmer climate than the control simulation it means that part of the surplus of energy compared to the preindustrial simulation, is coming from the higher water holding capacity of the warmer atmosphere. Both the CO_2 and non-CO_2 constraints cause a larger change in the Northern Hadley cell. When using the streamfunction for investigation of the Hadley circulation in the high CO_2 simulations, all models show a weakening intensity of the Southern cell and a shift of the Northern cell towards south. The intensity of the Northern cell is strengthening in HadCM3, MIROC, and COSMOS, while CESM and GFDL show a slight weakening (see Table 2). Figure 6 shows this exemplarily for the simulation GFDL. The southern cell is decreasing in intensity with the CO_2 rise, while the northern cell is expanding, mostly southward, and slightly increases in intensity. The southward expansion of the northern cell can be partially explained by the paleogeography. In the Eocene less continental land areas were located in the northern tropical belt. This could lead to a relative southward shift of the Intertropical Convergence Zone (ITCZ), given that during the summer half year the ITCZ travels poleward mostly over the continental areas. Nevertheless, the reason for the hemispheric asymmetry in overturned energy, intensity and position between the northern and southern Hadley cell due to CO_2 constraints is not entirely clear. These findings are in line with what we see in the modern day changing, warming climate. The 6th IPCC report states that a widening of the Hadley cells has been observed in the last decades, together with a strengthening of their circulation, especially in the Northern Hemisphere (Gulev et al., 2021).

Table 2

Streamfunction maximum and minimum values [kg/s] in the different models and simulations, indicating the intensity of each Hadley cell.

	CESM		GFDL		HadCM3		COSMOS		MIROC	
	South	North	South	North	South	North	South	North	South	North
piControl	1,0E+11	-8,8E+10	7,8E+10	-8,2E+10	9,2E+10	-9,6E+10	9,1E+10	-7,3E+10	1,1E+11	-7,3E+10
1xCO_2	6,1E+10	-7,4E+10	6,7E+10	-7,6E+10	9,0E+10	-1,4E+11	8,7E+10	-9,2E+10	9,2E+10	-8,8E+10
3xCO_2	5,5E+10	-6,7E+10	5,1E+10	-6,8E+10	7,9E+10	-1,3E+11	8,1E+10	-8,6E+10	8,4E+10	-9,9E+10
6xCO_2	5,4E+10	-6,6E+10	4,2E+10	-6,5E+10						

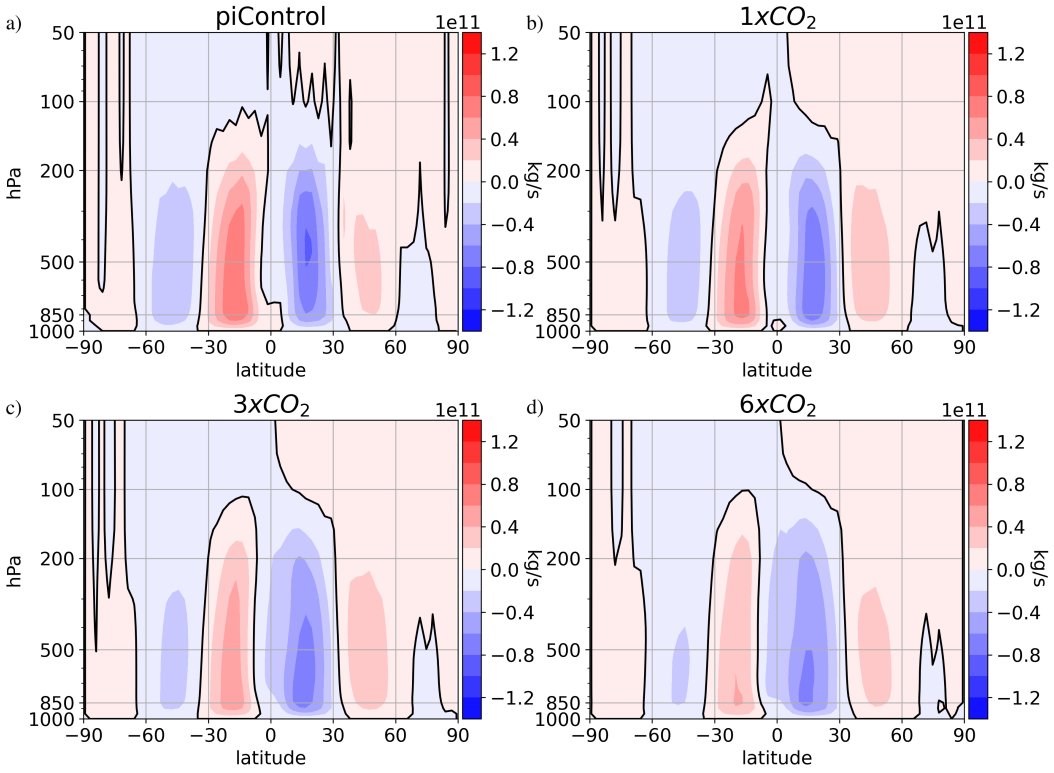

Figure 6. Cross section of the annual mean meridional streamfunction in the (a) preindustrial control, (b) 1xCO_2 , (c) 3xCO_2 , and (d) 6xCO_2 simulations of the GFDL model.

4.2 Monsoon

In the subtropics the transport via moist stationary eddies represents the heat transport by monsoon systems. The analysis of the non-CO_2 effects showed a decrease in their transport in the Northern Hemisphere and the CO_2 effects analysis showed an increase in transport with the CO_2 rise. Thus, we investigated the monsoon area to better evaluate these changes. The monsoon area is defined by a precipitation index in all simulations.

In Figure 7 the monsoon areas are plotted from the CESM preindustrial 1x, 3x and 6xCO_2 concentration simulation. Paleogeography plays an important role in defining monsoon areas as is shown by the smaller monsoon area in the early Eocene set-up than in the preindustrial. From the preindustrial to the 1xCO_2 simulations, the percentage of monsoon areas decreases in all models (see Table 3). The mean of the ensemble shows that in the preindustrial simulations the monsoon covers 18.7% of the globe, while in the 1xCO_2 this area is reduced to 14.8%. This correlates well with the slight decrease in the transport of moist stationary eddies in the subtropics (Fig. 2d). From the 1x to the 3x and to the 6xCO_2 simulations (for CESM), the monsoon area increases with higher CO_2 values (Figure 7). This also correlates well with the results seen in the transport figures, where there is an increase in moist stationary eddy transport in the subtropics (Figure 3d and 4d). The only exception from the increase of monsoon area with CO_2 rise, is GFDL with a decrease in monsoon area from the 3x to the 6xCO_2 simulation.

When comparing the preindustrial climate to the EECO, namely the preindustrial

simulations to the 6xCO_2 simulations for CESM and GDFL simulations, we see that the effect of the non-CO_2 constraints (smaller monsoon area in the Eocene) and the effect of the CO_2 forcing (higher water holding capacity of the warmer atmosphere) compensate each other in terms of the energy being transported. This agrees well with the findings of Licht et al. (2014), who investigated proxy data from Asia in the late Eocene (gastropod shells and mammal teeth from Myanmar, and aeolian dust deposition in northwest China) and found monsoon like patterns in rainfall and wind. They also concluded that the enhanced greenhouse gas concentrations compensated the negative effect of lower Tibetan relief on precipitation, which reduces the East Asian monsoon strength (Tang et al., 2013). In summary, when comparing present and EECO monsoon systems from the energetic point of view, there is no large difference (Figure 5d), nevertheless the reason for this is due to compensating mechanisms. Note that this does not indicate that there is no significant change in monsoon precipitation intensity.

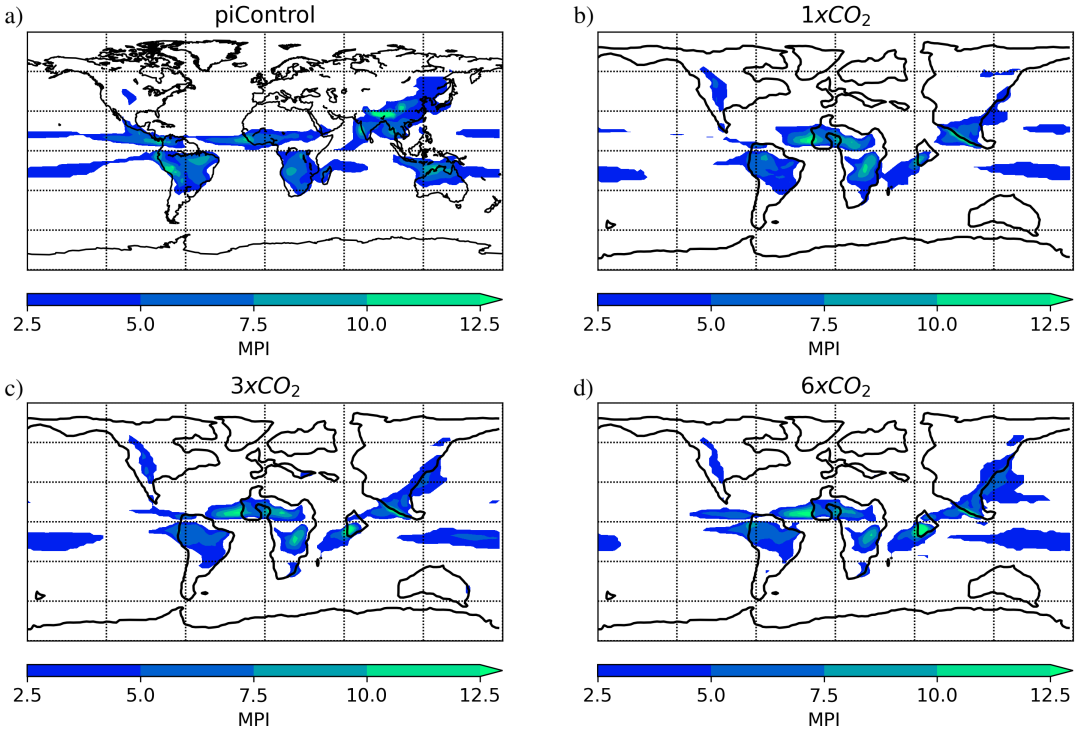

Figure 7. Monsoon area defined by the Monsoon Precipitation Index (MPI) with the unit of mm/day : a) preindustrial control b) 1xCO_2 c) 3xCO_2 and d) 6xCO_2 simulation of the CESM model.

Table 3

Global monsoon area in percentages in the different models and simulations.

	CESM	GFDL	HadCM3	MIROC	COSMOS	ENS
piControl	18.83	21.87	17.97	16.36	18.45	18.70
1xCO_2	14.61	19.17	13.59	10.47	16.43	14.85

3xCO_2	14.91	19.95	14.26	12.75	22.43	16.86
6xCO_2	15.42	18.04	-	-	-	16.73

636

637 4.3 Midlatitude cyclones

638 We found that in the paleo set up even without the CO_2 increase, more energy is being
639 transported via midlatitude cyclones especially in the Northern Hemisphere (Figure 2b). This can
640 be explained by an increase in semi-permanent low pressure systems, in other name centers of
641 action, in the Eocene simulations. In Figure 8 the sea level pressure anomalies are representing
642 these centers of action. In the Northern Hemisphere in the preindustrial simulation one can
643 identify two main low pressure systems during winter (Figure 8a), the Icelandic and the Aleutian
644 lows, while in the Eocene even four low pressure centers can be identified. We call these the
645 Icelandic, the Aleutian, the Gulf of Alaska and the Eurasian Low (Figure 8c).

646 The development of these semi-permanent pressure features is connected to the thermal
647 contrast between the ocean and the continent during winter, due to the different heat capacity of
648 land and sea. This also explains why the semi-permanent pressure systems develop differently in
649 the paleo set up. In the Eocene world there was a wider Pacific basin and a narrower Atlantic
650 basin together with the existence of the Turgai Sea or West Siberian Sea, an epicontinental sea
651 separating Europe from Asia. The existence of the West Siberian Sea, which is located in the
652 northern midlatitudes, lead, in the models, to the development of an Eurasian Low pressure
653 system that is not in present in the modern times. The wider Pacific basin and the presence of the
654 Bering land bridge lead, in the models, to a split in the Aleutian Low, so in the Eocene both an
655 Aleutian Low and a Gulf of Alaska Low are present in the simulations. In the Southern
656 Hemisphere the position of the Antarctic continent did not change much and, thus, the pressure
657 systems in the models developed similarly as in the present climate (Figure 8 b and d).

658 We hypothesize that the increase in the energy transport via transient eddies in the
659 paleosimulations are due to the increase in cyclonic activity due to more semi-permanent low
660 pressure systems over the northern midlatitudes. This can mean more and/or deeper cyclones
661 than in the present climate. To quantitatively assess this, the model output in our study with the
662 monthly temporal resolution is insufficient.

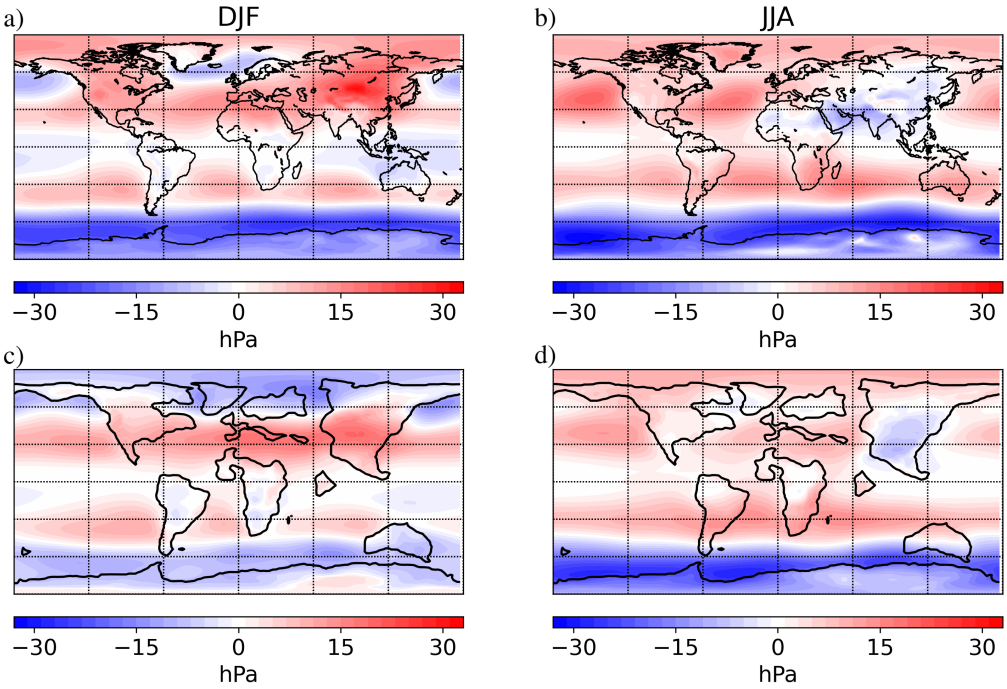

Figure 8. Winter (left) and summer (right) sea-level pressure anomaly in the a) b) preindustrial control and c) d) 1xCO_2 paleosimualtion of the CESM model.

5 Conclusions

In this study we calculated and analyzed the meridional heat transport and its partition in the atmosphere in climate model simulations of the preindustrial and the Early Eocene Climatic Optimum (EECO). We used simulations from five climate models (CESM, COSMOS, GFDL, HadCM3, and MIROC) provided by the DeepMIP community. The transport values are calculated from monthly mean data, and we distinguish between the different physical mechanisms, which transport energy in the atmosphere. The impacts of the non-CO_2 related conditions (paleogeography, vegetation, no continental ice sheets) and the CO_2 concentration forcing on the transport processes are calculated first separately, and then in combination, to allow a full comparison of heat transport in the preindustrial and early Eocene. The transport processes via the Hadley cell, the monsoon systems and the midlatitude cyclones are analyzed in more detail as these large-scale circulation patterns are identified as being different in the EECO compared to present day.

Our first research question investigates the DeepMIP models' skill in capturing the characteristics of transport processes in the preindustrial simulations (section 4.1). Overall, the DeepMIP ensemble mean and the reanalysis transport values show good agreement. Only the Southern Hemispheric tropical MOC transport shows marked differences, but due to two compensating mechanisms the overall atmospheric heat transport is still similar between the reanalysis and the multi-model mean.

The impacts of non-CO_2 constraints (paleogeography, vegetation, no continental ice sheet) on the different transport processes show hemispheric asymmetry. In the 1xCO_2 Eocene simulations the total poleward MHT is smaller in the Northern Hemisphere but larger in the

Southern Hemisphere. This is mainly due to the same change in oceanic transport. This shift in oceanic transport towards the South Pole is in line with the strong Southern Hemisphere-driven oceanic overturning circulation of the Eocene, found in the DeepMIP models (Zhang et al. (2022). Considering the different physical processes most notable is the extra heat transport by transient eddies in the midlatitudes, which is compensated by a loss in energy transport via stationary eddies. The increase in cyclonic heat transport is explained by changes in paleogeography. The existence of an extra epicontinental sea at the north midlatitudes, with possible high land-sea thermal contrast, results in a semi-permanent pressure system, which impacts the transient eddies at the midlatitudes. Also, the wide Pacific basin results in a split in the Aleutian Low. Thus, in the end during the Eocene winter there were probably 4 semi-permanent low pressure systems present at the northern midlatitudes as opposed to the only two in present day climate. The increase in semi-permanent lows likely results in an increase in cyclone numbers as well, but to quantify this, one needs high temporal resolution output from the models. A decrease in North Hemispheric monsoon latent heat transport, is also linked to the change in topography, since the location of land areas highly determines the monsoon area.

Transport changes, which are solely due to CO_2 increases in the 3x and 6x CO_2 EECO simulations, are especially relevant to better understand and predict changes under future climate change. We find that with increasing CO_2 concentrations, the atmosphere transports more heat poleward, while the ocean transports the same amount or less. The results also show that the Hadley cell overturns more heat on the northern side of the Equator more than on the southern side. Also, monsoon systems transport more latent heat from the subtropics to the higher latitudes. This indicates that with CO_2 rise the hydrological cycle intensifies. This agrees well with what have been found in our current changing climate. At the end of the 20th century the Hadley circulation is shown to be strengthening particularly in the Northern Hemisphere, while the global monsoon precipitation shows a positive trend in the Northern Hemisphere (Gulev et al., 2021).

Our third research question considers the total change between the preindustrial control and EECO simulations, and asks which physical processes are affected the most. In our results we see more changes in the Northern Hemisphere, where the atmosphere transports more heat poleward while the ocean compensates this with less poleward heat transport. We found an increase in latent heat transport towards the polar regions in both hemispheres midlatitudes in the EECO climate, and a decrease in poleward dry static energy transport, same results as Heinemann et al. (2009). The increase in latent heat transport is connected to the intense polar amplification of the EECO world. From the effected large scale circulation patterns, the Hadley cell changes both under the CO_2 and non-CO_2 constraints, with an asymmetric shift. More energy is being overturned in the northern cell, and less in the southern one, while the net poleward MOC heat transport stays close to the control simulation. Monsoon systems are also affected by both the non-CO_2 and CO_2 constraint, but in an opposite way. We found smaller monsoon areas in the Eocene, due to the different topography, while at a higher CO_2 concentration, the warmer atmosphere's higher water holding capacity means that more heat is transported poleward by the monsoons. At the midlatitudes cyclones' heat transport increase mainly in the Northern Hemisphere, due to the before mentioned topography differences.

In summary we found that transport processes indicate a more intense hydrological cycle and also polar amplification in the warmer EECO compared to the present-day climate. We identified which processes are affected by the Eocene boundary conditions and which are

sensitive to the CO_2 increase. The different boundary conditions cause more southward transport in the ocean which is only partially compensated by the atmosphere. The Eocene set up increases the heat transport of northern midlatitude cyclones and decreases the global monsoon area. The CO_2 increase, on the other hand causes an increase in poleward atmospheric heat transport. Regarding the large scale circulation patterns the CO_2 increase results in an increase in the latent heat transport of monsoon systems and more overturning heat in the Hadley circulation, although the net poleward transport of the Hadley cells is stable. Nevertheless, there is an asymmetry between the northern and southern Hadley cell, with larger changes in the northern cell. A more detailed analysis of the largescale circulation patterns of the Eocene climate, in higher temporal and spatial resolution model results, and their comparison to proxy data, is the focus of our further research.

Acknowledgments

This research was funded through the VeWA consortium (Past Warm Periods as Natural Analogues of our high-CO_2 Climate Future) by the LOEWE programme of the Hessen Ministry of Higher Education, Research and the Arts, Germany. The CESM project is supported primarily by the National Science Foundation (NSF). This material is based upon work supported by the National Center for Atmospheric Research, which is a major facility sponsored by the NSF under Cooperative Agreement No. 1852977. The GFDL simulations were performed using resources from the Swedish National Infrastructure for Computing (SNIC) at the National Supercomputer Centre (NSC), partially funded by the Swedish Research Council grant 2018-05973. ADB acknowledges support from Swedish Research council grant 2020-04791. SS acknowledges funding from the NERC SWEET grant (grant no. NE/P01903X/1). The MIROC4m simulations were performed on the Earth Simulator supercomputer and funded by Kakenhi grants 17H06104 and 17H06323. The results contain modified Copernicus Climate Change Service information 2022. Neither the European Commission nor ECMWF is responsible for any use that may be made of the Copernicus information or data it contains.

Open Research

The DeepMIP PI and Eocene simulations are available by following the instructions at **https://www.deepmip.org/data-eocene/**; please see (Lunt et al., 2021). Hersbach, H. et al., (2019) was downloaded from the Copernicus Climate Change Service (C3S) Climate Data Store.

References

Anagnostou, E., John, E. H., Babila, T. L., Sexton, P. F., Ridgwell, A., Lunt, D. J., Pearson, P. N., Chalk, T. B., Pancost, R. D., & Foster, G. L. (2020). Proxy evidence for state-dependence of climate sensitivity in the Eocene greenhouse. *Nature Communications*, *11*(1). https://doi.org/10.1038/s41467-020-17887-x

Barron, E. J. (1987). Eocene equator-to-pole surface ocean temperatures: A significant climate problem? *Paleoceanography*, *2*(6), 729–739.

https://doi.org/https://doi.org/10.1029/PA002i006p00729

Bjerknes, J. (1964). Atlantic air-sea interaction. *Advances in Geophysics*, *10*, 1–82. https://doi.org/10.1016/S0065-2687(08)60005-9

Chan, W.-L., & Abe-Ouchi, A. (2020). Pliocene Model Intercomparison Project (PlioMIP2) simulations using the Model for Interdisciplinary Research on Climate (MIROC4m). *Climate of the Past*, *16*(4), 1523–1545. https://doi.org/10.5194/cp-16-1523-2020

Delworth, T. L., Broccoli, A. J., Rosati, A., Stouffer, R. J., Balaji, V., Beesley, J. A., Cooke, W. F., Dixon, K. W., Dunne, J., Dunne, K. A., Durachta, J. W., Findell, K. L., Ginoux, P., Gnanadesikan, A., Gordon, C. T., Griffies, S. M., Gudgel, R., Harrison, M. J., Held, I. M., … Zhang, R. (2006). GFDL ' s CM2 Global Coupled Climate Models . Part I : Formulation and. *Journal of Climate*, *19*, 643–674.

Donohoe, A., Armour, K. C., Roe, G. H., Battisti, D. S., & Hahn, L. (2020). The partitioning of meridional heat transport from the last glacial maximum to CO2 quadrupling in coupled climate models. *Journal of Climate*, *33*(10), 4141–4165. https://doi.org/10.1175/JCLI-D-19-0797.1

Evans, D., Sagoo, N., Renema, W., Cotton, L. J., Müller, W., Todd, J. A., Saraswati, P. K., Stassen, P., Ziegler, M., Pearson, P. N., Valdes, P. J., & Affek, H. P. (2018). Eocene greenhouse climate revealed by coupled clumped isotope-Mg/Ca thermometry. *Proceedings of the National Academy of Sciences of the United States of America*, *115*(6), 1174–1179. https://doi.org/10.1073/pnas.1714744115

Forster, P., Storelvmo, T., Armour, K., Collins, W., Dufresne, J.-L., Frame, D., Lunt, D. J., Mauritsen, T., Palmer, M. D., Watanabe, M., Wild, M., & Zhang, H. (2021). Earth's energy budget, climate feedbacks, and climate sensitivity. In V. Masson-Delmotte, P. Zhai, A. Pirani, S. L. Connors, C. Péan, S. Berger, N. Caud, Y. Chen, L. Goldfarb, M. I. Gomis, M. Huang, K. Leitzell, E. Lonnoy, J. B. R. Matthews, T. K. Maycock, T. Waterfield, O. Yelek, R. Yu, & B. Zhou (Eds.), *Climate Change 2021: The Physical Science Basis. Contribution of Working Group I to the Sixth Assessment Report of the Intergovernmental Panel on Climate Change* (pp. 923–1054). Cambridge University Press. https://doi.org/10.12006/j.issn.1673-1719.2021.191

Gulev, S. K., Thorne, P. W., Ahn, J., Dentener, F. J., Domingues, C. M., Gerland, S., Gong, D., Kaufman, D. S., Nnamchi, H. C., Quaas, J., Rivera, J. A., Sathyendranath, S., Smith, S. L., Trewin, B., Schuckmann, K. von, & Vose, R. S. (2021). Changing State of the Climate System. In V. Masson-Delmotte, P. Zhai, A. Pirani, S. L. Connors, C. Péan, S. Berger, N. Caud, Y. Chen, L. Goldfarb, M. I. Gomis, M. Huang, K. Leitzell, E. Lonnoy, J. B. R. Matthews, T. K. Maycock, T. Waterfield, O. Yelek, R. Yu, & B. Zhou (Eds.), *Climate Change 2021: The Physical Science Basis. Contribution of Working Group I to the Sixth Assessment Report of the Intergovernmental Panel on Climate Change* (pp. 287–422). Cambridge University Press. https://doi.org/10.1017/9781009157896.004.288

Hasumi, H. (2000). *CCSR Ocean Component Model (COCO) Version 2.1, Technical Report,*.

Heinemann, M., Jungclaus, J. H., & Marotzke, J. (2009). Warm Paleocene/Eocene climate as simulated in ECHAM5/MPI-OM. *Climate of the Past*, *5*(4), 785–802. https://doi.org/10.5194/cp-5-785-2009

817 Held, I. M. (2001). The partitioning of the poleward energy transport between the tropical ocean
818 and atmosphere. *Journal of the Atmospheric Sciences*, *58*(8), 943–948.
819 https://doi.org/10.1175/1520-0469(2001)058<0943:TPOTPE>2.0.CO;2

820 Herold, N., Buzan, J., Seton, M., Goldner, A., Green, J. A. M., Müller, R. D., Markwick, P., &
821 Huber, M. (2014). A suite of early Eocene (~ 55 Ma) climate model boundary conditions.
822 *Geoscientific Model Development*, *7*(5), 2077–2090. https://doi.org/10.5194/gmd-7-2077-
823 2014

824 Hersbach, H., Bell, B., Berrisford, P., Biavati, G., Horányi, A., Muñoz Sabater, J., Nicolas, J.,
825 Peubey, C., Radu, R., Rozum, I., Schepers, D., Simmons, A., Soci, C., Dee, D., & Thépaut,
826 J.-N. (2019a). *ERA5 monthly averaged data on pressure levels from 1959 to present.*
827 *Copernicus Climate Change Service (C3S) Climate Data Store (CDS). (Accessed on < 24-*
828 *AUG-2022 >)*. https://doi.org/10.24381/cds.6860a573

829 Hersbach, H., Bell, B., Berrisford, P., Biavati, G., Horányi, A., Muñoz Sabater, J., Nicolas, J.,
830 Peubey, C., Radu, R., Rozum, I., Schepers, D., Simmons, A., Soci, C., Dee, D., & Thépaut,
831 J.-N. (2019b). *ERA5 monthly averaged data on single levels from 1959 to present.*
832 *Copernicus Climate Change Service (C3S) Climate Data Store (CDS). (Accessed on < 24-*
833 *AUG-2022 >),*. https://doi.org/10.24381/cds.f17050d7

834 Hersbach, Hans, Bell, B., Berrisford, P., Hirahara, S., Horányi, A., Muñoz-Sabater, J., Nicolas,
835 J., Peubey, C., Radu, R., Schepers, D., Simmons, A., Soci, C., Abdalla, S., Abellan, X.,
836 Balsamo, G., Bechtold, P., Biavati, G., Bidlot, J., Bonavita, M., … Thépaut, J. N. (2020).
837 The ERA5 global reanalysis. *Quarterly Journal of the Royal Meteorological Society*,
838 *146*(730), 1999–2049. https://doi.org/10.1002/qj.3803

839 Hollis, C. J., Dunkley Jones, T., Anagnostou, E., Bijl, P. K., Cramwinckel, M. J., Cui, Y.,
840 Dickens, G. R., Edgar, K. M., Eley, Y., Evans, D., Foster, G. L., Frieling, J., Inglis, G. N.,
841 Kennedy, E. M., Kozdon, R., Lauretano, V., Lear, C. H., Littler, K., Lourens, L., … Lunt,
842 D. J. (2019). The DeepMIP contribution to PMIP4: Methodologies for selection,
843 compilation and analysis of latest Paleocene and early Eocene climate proxy data,
844 incorporating version 0.1 of the DeepMIP database. *Geoscientific Model Development*,
845 *12*(7), 3149–3206. https://doi.org/10.5194/gmd-12-3149-2019

846 Huber, M., & Sloan, L. C. (2001). Heat transport, deep waters, and thermal gradients: Coupled
847 simulation of an Eocene greenhouse climate. *Geophysical Research Letters*, *28*(18), 3481–
848 3484. https://doi.org/10.1029/2001GL012943

849 Huber, Matthew, & Nof, D. (2006). The ocean circulation in the southern hemisphere and its
850 climatic impacts in the Eocene. *Palaeogeography, Palaeoclimatology, Palaeoecology*,
851 *231*(1–2), 9–28. https://doi.org/10.1016/j.palaeo.2005.07.037

852 Hurrell, J. W., Holland, M. M., Gent, P. R., Ghan, S., Kay, J. E., Kushner, P. J., Lamarque, J. F.,
853 Large, W. G., Lawrence, D., Lindsay, K., Lipscomb, W. H., Long, M. C., Mahowald, N.,
854 Marsh, D. R., Neale, R. B., Rasch, P., Vavrus, S., Vertenstein, M., Bader, D., … Marshall,
855 S. (2013). The community earth system model: A framework for collaborative research.
856 *Bulletin of the American Meteorological Society*, *94*(9), 1339–1360.
857 https://doi.org/10.1175/BAMS-D-12-00121.1

858 Hutchinson, D. K., Coxall, H. K., O′Regan, M., Nilsson, J., Caballero, R., & de Boer, A. M.
859 (2019). Arctic closure as a trigger for Atlantic overturning at the Eocene-Oligocene

Transition. *Nature Communications*, *10*(1). https://doi.org/10.1038/s41467-019-11828-z

Hutchinson, D. K., De Boer, A. M., Coxall, H. K., Caballero, R., Nilsson, J., & Baatsen, M. (2018). Climate sensitivity and meridional overturning circulation in the late Eocene using GFDL CM2.1. *Climate of the Past*, *14*(6), 789–810. https://doi.org/10.5194/cp-14-789-2018

Inglis, G. N., Bragg, F., Burls, N., Evans, D., Foster, G., Huber, M., Lunt, D., Siler, N., Steinig, S., Wilkinson, R., Anagnostou, E., Cramwinckel, M., Hollis, C., Pancost, R., & Tierney, J. E. (2020). Global mean surface temperature and climate sensitivity of the EECO, PETM and latest Paleocene. *Climate of The Past Discussions*, *44*(January), 1–43. https://doi.org/10.31223/osf.io/8527z

IPCC. (2021). *Annex V : Monsoons* (pp. 2193–2204). https://doi.org/10.1017/9781009157896.019.2193

Kiehl, J. T., & Shields, C. A. (2013). Sensitivity of the palaeocene-eocene thermal maximum climate to cloud properties. *Philosophical Transactions of the Royal Society A: Mathematical, Physical and Engineering Sciences*, *371*(2001). https://doi.org/10.1098/rsta.2013.0093

Kitoh, A., Endo, H., Krishna Kumar, K., Cavalcanti, I. F. A., Goswami, P., & Zhou, T. (2013). Monsoons in a changing world: A regional perspective in a global context. *Journal of Geophysical Research Atmospheres*, *118*(8), 3053–3065. https://doi.org/10.1002/jgrd.50258

Krapp, M., & Jungclaus, J. H. (2011). The Middle Miocene climate as modelled in an atmosphere-ocean-biosphere model. *Climate of the Past*, *7*(4), 1169–1188. https://doi.org/10.5194/cp-7-1169-2011

Licht, A., Van Cappelle, M., Abels, H. A., Ladant, J. B., Trabucho-Alexandre, J., France-Lanord, C., Donnadieu, Y., Vandenberghe, J., Rigaudier, T., Lécuyer, C., Terry, D., Adriaens, R., Boura, A., Guo, Z., Soe, A. N., Quade, J., Dupont-Nivet, G., & Jaeger, J. J. (2014). Asian monsoons in a late Eocene greenhouse world. *Nature*, *513*(7519), 501–506. https://doi.org/10.1038/nature13704

Lunt, D. J., Bragg, F., Chan, W.-L., Hutchinson, D. K., Ladant, J. B., Morozova, P., Niezgodzki, I., Steinig, S., Zhang, Z., Zhu, J., Abe-Ouchi, A., Anagnostou, E., De Boer, A. M., Coxall, H. K., Donnadieu, Y., Foster, G., Inglis, G. N., Knorr, G., Langebroek, P. M., … Otto-Bliesner, B. L. (2021). DeepMIP: Model intercomparison of early Eocene climatic optimum (EECO) large-scale climate features and comparison with proxy data. *Climate of the Past*, *17*(1), 203–227. https://doi.org/10.5194/cp-17-203-2021

Lunt, D. J., Huber, M., Anagnostou, E., Baatsen, M. L. J., Caballero, R., DeConto, R., Dijkstra, H. A., Donnadieu, Y., Evans, D., Feng, R., Foster, G. L., Gasson, E., Von Der Heydt, A. S., Hollis, C. J., Inglis, G. N., Jones, S. M., Kiehl, J., Turner, S. K., Korty, R. L., … Zeebe, R. E. (2017). The DeepMIP contribution to PMIP4: Experimental design for model simulations of the EECO, PETM, and pre-PETM (version 1.0). *Geoscientific Model Development*, *10*(2), 889–901. https://doi.org/10.5194/gmd-10-889-2017

Marshall, J., Donohoe, A., Ferreira, D., & McGee, D. (2014). The ocean's role in setting the mean position of the Inter-Tropical Convergence Zone. *Climate Dynamics*, *42*(7–8), 1967–1979. https://doi.org/10.1007/s00382-013-1767-z

Marsland, S. J., Haak, H., Jungclaus, J. H., Latif, M., & Röske, F. (2003). The Max-Planck-

902 Institute global ocean/sea ice model with orthogonal curvilinear coordinates. *Ocean*
903 *Modelling*, *5*(2), 91–127. https://doi.org/10.1016/S1463-5003(02)00015-X

904 Masuda, K. (1988). Meridional heat transport by the atmosphere and the ocean: analysis of
905 FGGE data. *Tellus, Series A*, *40 A*(4), 285–302. https://doi.org/10.3402/tellusa.v40i4.11801

906 Outten, S., Esau, I., & Otterå, O. H. (2018). Bjerknes compensation in the CMIP5 climate
907 models. *Journal of Climate*, *31*(21), 8745–8760. https://doi.org/10.1175/JCLI-D-18-0058.1

908 Roeckner, E., Bäuml, G., Bonaventura, L., , Brokopf, R., Esch, M., , Giorgetta, M., Hagemann,
909 S., Kirchner, I., Kornbleuh, L., , Manzini, E., Rhodin, A., Schlese, U., Schulzweida, U., &
910 Tompkins, A. (2003). *The atmospheric general circulation model ECHAM 5. PART I:*
911 *Model description* (Issue 140).

912 Sloan, L. C., Walker, J. C. G., & Moore Jr., T. C. (1995). Possible role of oceanic heat transport
913 in Early Eocene climate. *Paleoceanography*, *10*(2), 347–356.
914 https://doi.org/https://doi.org/10.1029/94PA02928

915 Smith, R. S., Dubois, C., & Marotzke, J. (2006). Global climate and ocean circulation on an
916 aquaplanet ocean-atmosphere general circulation model. *Journal of Climate*, *19*(18), 4719–
917 4737. https://doi.org/10.1175/JCLI3874.1

918 Stepanek, C., & Lohmann, G. (2012). Modelling mid-pliocene climate with COSMOS.
919 *Geoscientific Model Development*, *5*(5), 1221–1243. https://doi.org/10.5194/gmd-5-1221-
920 2012

921 Stone, P. H. (1978). Constraints on Dynamical Transports of Energy on a Spherical Planet.
922 *Dynamics of Atmospheres and Oceans*, *2*, 123–139.

923 Takata, K., Emori, S., & Watanabe, T. (2003). Development of the minimal advanced treatments
924 of surface interaction and runoff. *Global and Planetary Change*, *38*(1–2), 209–222.
925 https://doi.org/10.1016/S0921-8181(03)00030-4

926 Tang, H., Eronen, J. T., Micheels, A., & Ahrens, B. (2013). Strong interannual variation of the
927 Indian summer monsoon in the Late Miocene. *Climate Dynamics*, *41*(1), 135–153.
928 https://doi.org/10.1007/s00382-012-1655-y

929 Valdes, P. J., Armstrong, E., Badger, M. P. S., Bradshaw, C. D., Bragg, F., Crucifix, M., Davies-
930 Barnard, T., Day, J., Farnsworth, A., Gordon, C., Hopcroft, P. O., Kennedy, A. T., Lord, N.
931 S., Lunt, D. J., Marzocchi, A., Parry, L. M., Pope, V., Roberts, W. H. G., Stone, E. J., …
932 Williams, J. H. T. (2017). The BRIDGE HadCM3 family of climate models:
933 HadCM3@Bristol v1.0. *Geoscientific Model Development*, *10*(10), 3715–3743.
934 https://doi.org/10.5194/gmd-10-3715-2017

935 Wills, R. C. J., White, R. H., & Levine, X. J. (2019). Northern Hemisphere Stationary Waves in
936 a Changing Climate. *Current Climate Change Reports*, *5*(4), 372–389.
937 https://doi.org/10.1007/s40641-019-00147-6

938 Xian, T., Xia, J., Wei, W., Zhang, Z., Wang, R., Wang, L. P., & Ma, Y. F. (2021). Is hadley cell
939 expanding? *Atmosphere*, *12*(12), 1–31. https://doi.org/10.3390/atmos12121699

940 Yang, H., Zhao, Y., Liu, Z., Li, Q., He, F., & Zhang, Q. (2015). Heat transport compensation in
941 atmosphere and ocean over the past 22,000 years. *Scientific Reports*, *5*, 1–11.
942 https://doi.org/10.1038/srep16661

Zhang, Y., de Boer, A. M., Lunt, D. J., Hutchinson, D. K., Ross, P., van de Flierdt, T., Sexton, P., Coxall, H. K., Steinig, S., Ladant, J. B., Zhu, J., Donnadieu, Y., Zhang, Z., Chan, W.-L., Abe-Ouchi, A., Niezgodzki, I., Lohmann, G., Knorr, G., Poulsen, C. J., & Huber, M. (2022). Early Eocene Ocean Meridional Overturning Circulation: The Roles of Atmospheric Forcing and Strait Geometry. *Paleoceanography and Paleoclimatology*, *37*(3), 1–22. https://doi.org/10.1029/2021PA004329